



Experimental Observation of Large Chern Numbers in Photonic Crystals

Scott A. Skirlo,^{1,*} Ling Lu,^{1,†} Yuichi Igarashi,^{1,2} Qinghui Yan,^{1,3} John Joannopoulos,¹ and Marin Soljačić¹

¹*Department of Physics, Massachusetts Institute of Technology, Cambridge, Massachusetts 02139, USA*

²*Smart Energy Research Laboratories, NEC Corporation, 34 Miyukigaoka, Tsukuba, Ibaraki 305-8501, Japan*

³*The Electromagnetics Academy at Zhejiang University, Zhejiang University, Hangzhou 310027, China*

(Received 15 April 2015; revised manuscript received 22 September 2015; published 14 December 2015)

Despite great interest in the quantum anomalous Hall phase and its analogs, all experimental studies in electronic and bosonic systems have been limited to a Chern number of one. Here, we perform microwave transmission measurements in the bulk and at the edge of ferrimagnetic photonic crystals. Band gaps with large Chern numbers of 2, 3, and 4 are present in the experimental results, which show excellent agreement with theory. We measure the mode profiles and Fourier transform them to produce dispersion relations of the edge modes, whose number and direction match our Chern number calculations.

DOI: 10.1103/PhysRevLett.115.253901

PACS numbers: 42.79.Ta, 42.70.Qs, 42.79.Fm, 42.79.Gn

The Chern number [1] is an integer defining the topological phase in the quantum Hall effect (QHE) [2], which determines the number of topologically protected chiral edge modes. The quantum anomalous Hall effect (QAHE) possesses these same properties as an intrinsic property of the band structure with time reversal symmetry breaking [3,4]. Recent experiments have discovered the QAHE and its analogs in ferrimagnetic photonic crystals [5], magnetically doped thin films [6], and ultracold fermion lattices [7]. However, the Chern numbers observed in all of these systems were limited to ± 1 . Finding larger Chern numbers would fundamentally expand the known topological phases [8–12].

Here, we provide the first explicit experimental observation of Chern numbers of magnitude 2, 3, and 4, by measuring bulk transmission, edge transmission, and the edge-mode dispersion relations in a ferrimagnetic photonic crystal. The excellent agreement between the experiment and the modeling allows us to identify various topological band gaps and map out the dispersion relations of one-way edge modes for the first time in *any* QHE or QAHE system in nature.

In a 2D system one can realize bands with nonzero Chern numbers, and generate the QAHE, by applying a T -breaking perturbation [13–15]. The Chern number is defined as the integral of the Berry flux over the entire Brillouin zone. When connected bands are gapped by a T -breaking perturbation, the bands will exchange equal and opposite Berry flux at each degenerate point, with the total Berry flux exchanged determining the Chern number. For instance, two isolated bands connected by one pair of Dirac points gapped by T -breaking will acquire $\pm 2\pi$ Berry flux (π from each Dirac point) and a Chern number associated with the band gap (“gap Chern number”) of ± 1 . A general way to calculate the gap Chern number ($C_{\text{gap}} = \sum C_i$) is to sum the Chern numbers of all the bands below the band gap [16]. A band gap with $C_{\text{gap}} = 0$ is trivial, while a band gap with $C_{\text{gap}} \neq 0$ is topologically nontrivial.

In our previous theoretical study, we found that the magnitude of the gap Chern number can be increased above one by simultaneously gapping multiple sets of Dirac and quadratic degeneracies. If Berry flux from the gapped degeneracies adds constructively, C_{gap} can be large. In Fig. 1(a) we present a theoretical topological gap map for a 2D ferrimagnetic photonic crystal as a function of the externally applied magnetic field and the frequency, showing nontrivial band gaps with C_{gap} from -4 to 3. We studied this same square lattice in an experiment to verify these predictions.

The experimental configuration resembles a prior work which demonstrated $|C_{\text{gap}}| = 1$ [5]. A square lattice of ferrimagnetic garnet rods is placed between two conductive copper plates. This configuration forms a parallel-plate waveguide, with the electric field perpendicular to the plate. Since the electric field for the fundamental mode is constant as a function of height, this is equivalent to a 2D system. The modes in the photonic crystal are excited by antennas attached to the top plate and fed to a network analyzer. Around the boundary of the system, we placed an absorber to minimize reflections and outside interference. We include an overhead image of one of the crystals we constructed in Fig. 1(d).

To observe the QAHE analog in the experiment, we break T symmetry by applying a spatially uniform magnetic field to the ferrimagnetic garnet rods, which acquire off-diagonal imaginary parts in the permeability tensor [18]. Unlike electrons, the external magnetic field does not interact directly with photons. However, for this system, Maxwell’s equations can be written in the exact same form as the Schrödinger equation with a periodic vector potential [15]. This makes the system an analog of the QAHE. Our photonic crystals were placed in the Massachusetts Institute of Technology (MIT) cyclotron magnet, and the magnetic field was swept between 0.03 and 0.55 T to characterize the transmission of the photonic crystal as a function of the magnetic field and the frequency.

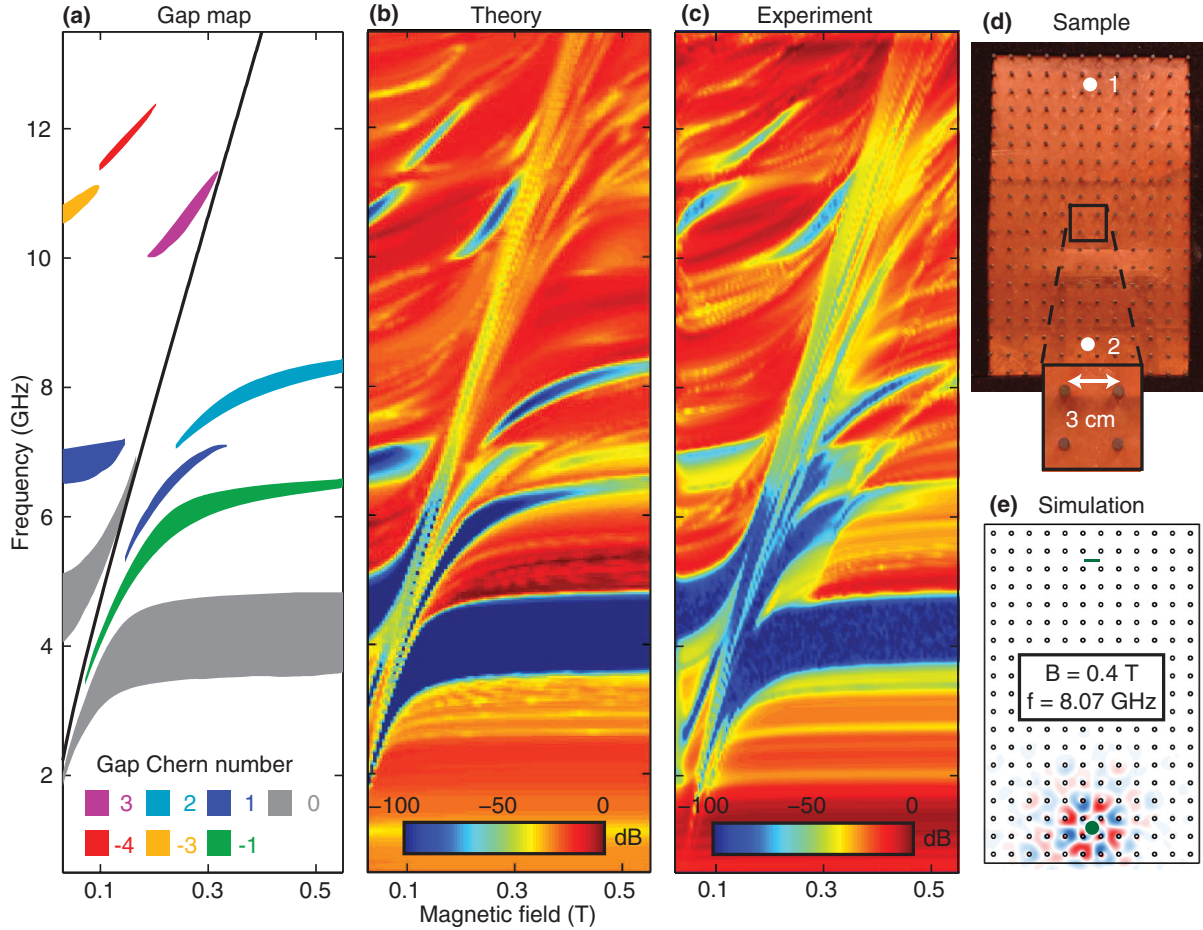


FIG. 1 (color online). Comparison of theoretical gap map and bulk transmission to experimental transmission measurement in a 2D ferrimagnetic photonic crystal. (a) Theoretical topological gap map as a function of the magnetic field and the frequency, with each band gap labeled by its gap Chern number. The diagonal black line indicates the resonance in the effective permeability (see the Supplemental Material [17]). (b) Theoretical bulk transmission. (c) Experimental bulk transmission. (d) Experimental configuration with the lattice geometry (top metal plate removed). The antenna locations are marked with 1 and 2. (e) Simulation geometry, with the green line representing the receiving antenna and the green circle representing the transmitting antenna.

We show the experimental transmission through a bulk photonic crystal in Fig. 1(c). Here, the color illustrates the amplitude of the transmission between the antennas in decibels [$S_{12} = 20 \log(E_{\text{in}}/E_{\text{out}})$]. In the plots there are several deep blue regions of low transmission that clearly correspond to the locations of band gaps in the gap map. The sweeping feature that extends diagonally across the figure is due to the gyromagnetic resonance of the ferrimagnetic garnet rods (see the Supplemental Material [17]). The resonant frequency of the effective permeability is plotted with a black line in Fig. 1(a).

In Fig. 1(b) we present the corresponding theoretical data for transmission through a lattice of the same size and dimension calculated with COMSOL. One of the transmission simulations is shown in Fig. 1(e). For direct comparison, the transmission data in Fig. 1(b) are plotted with the same color bar scale as the experiment in Fig. 1(c). The slight offset of about 0.04 T in the magnetic field

between the theoretical and experimental plots is caused by demagnetization (see the Supplemental Material [17]). Clearly, the theoretical and experimental transmissions bear strong resemblance to each other and the topological gap map, showing that a square lattice of ferrimagnetic rods can contain a wide variety of different C_{gap} numbers.

Several nontrivial band gaps in Fig. 1 and in the Supplemental Material [17] occur even at low magnetic fields. This indicates that topological effects can be achieved at low applied magnetic fields ($\sim 0.03 \text{ T}$) enabling various studies and applications. Furthermore, these same band gaps would remain open at zero external magnetic field by using ferrimagnetic materials with remanent magnetization [19]; this way, a future experiment could be performed even without external magnetic fields.

One-way edge modes are present at the boundary between two crystals with a nontrivial and a trivial band gap, respectively, or at the boundary between crystals with

nontrivial band gaps with different C_{gap} [4,20]. If the band gaps of two neighboring crystals overlap in frequency, the number of edge states in the shared frequency gap is determined by the difference between the gap Chern numbers of each crystal. The sign of this difference determines the directions of the edge states. This means that with the nontrivial band gaps we found, constructing one-way waveguides with up to seven modes is possible. If one of the materials is trivial ($C_{\text{gap}} = 0$), like metal or air, the number of edge states equals the gap Chern number of the crystal, with the sign of this number determining their directions.

To provide more evidence of the topological state of these band gaps and the one-way modes, we modified the setup to include a highly conductive copper boundary at the edge of the crystal. This boundary acts as a mirror with a

trivial band gap. We place two antennas near this edge on each side of the sample and measure the transmission between them. In Figs. 2(a) and 2(b) we present both the S_{12} and S_{21} parameters to describe the direction-dependent transmission of the edge modes along the metal boundary. S_{12} refers to exciting the second antenna and measuring with the first antenna, while S_{21} is the opposite.

The band gaps that are nontrivial ($C_{\text{gap}} \neq 0$) can be identified in Fig. 2 because they will have direction-dependent edge transmission. Specifically, the nontrivial band gaps measured in Fig. 1(c) will appear in either Fig. 2(a) or Fig. 2(b), but not both. We show this explicitly for the $C_{\text{gap}} = -4$ band gap by highlighting the direction-dependent transmission with gray boxes. This arises from the directional edge states as follows. In one direction, the group velocity of the edge modes is opposite that required

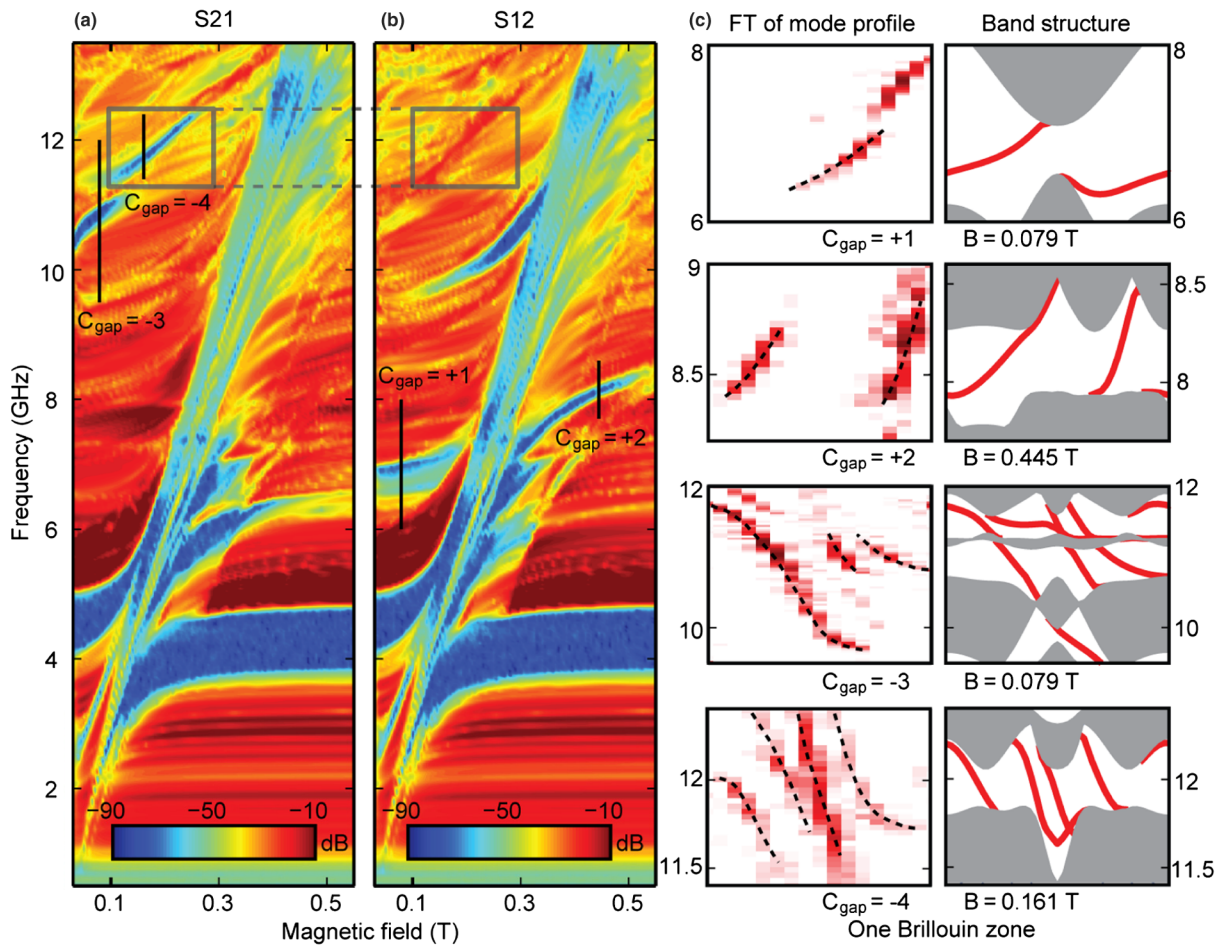


FIG. 2 (color online). Experimental edge transmission measurement and Fourier transform (FT) of mode profiles along the copper boundary. (a) S_{21} . (b) S_{12} . The band gaps that are nontrivial have direction-dependent edge transmission because the interface of a nontrivial band gap with a trivial band gap (copper boundary) supports one-way modes. In (a) and (b) this causes the nontrivial bulk band gaps from Fig. 1(c) to be present in one direction (e.g., S_{12}) and absent in the other (e.g., S_{21}), which we highlight for the $C_{\text{gap}} = -4$ band gap with black boxes. The trivial band gaps around 4 GHz do not support one-way modes, and so they do not exhibit direction-dependent transmission. (c) Experimental FT of edge-mode profiles and the theoretical edge band structures with the edge modes in red and the bulk bands in gray. The range of wave vectors included in both plots is the same and includes only one Brillouin zone. The number of one-way edge modes in both sets of panels agrees with $|C_{\text{gap}}|$ from Fig. 1(a), while the sign of C_{gap} is consistent with the theoretical group velocity (from the edge-mode dispersion) and the directional transmission in (a) and (b).

to travel to the receiving antenna, so the transmission measurement will record the bulk band gap. However, in the other direction, the group velocity of the edge modes is in the same direction as is required to get to the receiving antenna, so the band gap will appear to be nonexistent. Trivial band gaps ($C_{\text{gap}} = 0$) around 4 GHz do not support one-way edge modes and thus do not exhibit direction-dependent transmission at the edge.

To further study the topological nature of these band gaps, we measured the mode profile at the edge of the photonic crystal. We accomplished this by mounting one antenna for excitation to the lower plate, and another small dipole antenna for measurement to the upper plate [21]. During the measurement, the upper plate was translated a total of 47 cm in 2.5 mm steps. At each step both the phase and the amplitude of the electric field was recorded (see the Supplemental Material [17]). From this spatial data, the mode profile in the waveguide can be reconstructed. The Fourier transform of the mode profile produces the dispersion relation of the waveguide, which we present on the left-hand side of Fig. 2(c).

In Fig. 2(c) on the right-hand side, we include a comparison with the edge band calculations, with the bulk bands in gray and the edge modes in red. It is clear that the calculated edge-mode dispersion shows an excellent agreement with the dispersion relations extracted from experiments. The number of edge modes is equal to the gap Chern number for each inset. The sign of C_{gap} is consistent with the group velocity of the edge modes and agrees with the directional edge transmission data in Figs. 2(a) and 2(b). In the Supplemental Material [17] we present additional simulations validating these results for $C_{\text{gap}} = -3$ and -4 . These results constitute the first direct measurement of one-way edge-mode dispersion in any QHE system.

To further study the gap Chern numbers of the observed topological band gaps, we construct a topological one-way circuit [11]. As illustrated in Fig. 3(d), this consists of a $C_{\text{gap}} = 2$ ($a = 3.0$ cm) crystal and a $C_{\text{gap}} = 1$ ($a = 2.4$ cm) crystal, with a copper boundary on the edge. We present the design and calculations characterizing the $C_{\text{gap}} = 1$ crystal in the Supplemental Material [17], while the results from the $C_{\text{gap}} = 2$ crystal are shown in Figs. 1 and 2. From the rules described earlier, there will be two edge states flowing downwards between the metal boundary and the $C_{\text{gap}} = 2$ crystal, as indicated with arrows in Fig. 3(d). These edge states will “split” at the junction, with one edge state flowing away along the boundary between the $C_{\text{gap}} = 1$ and the $C_{\text{gap}} = 2$ crystal and the other continuing along the metal and $C_{\text{gap}} = 1$ crystal interface.

In Figs. 3(a)–3(c) we present the transmission between ports 1–3 and a fourth port located at the junction, as labeled in Fig. 3(d). The highlighted yellow region indicates the shared band gap between the $C_{\text{gap}} = 1$ crystal and the $C_{\text{gap}} = 2$ crystal. For each of the measurements, it is clear

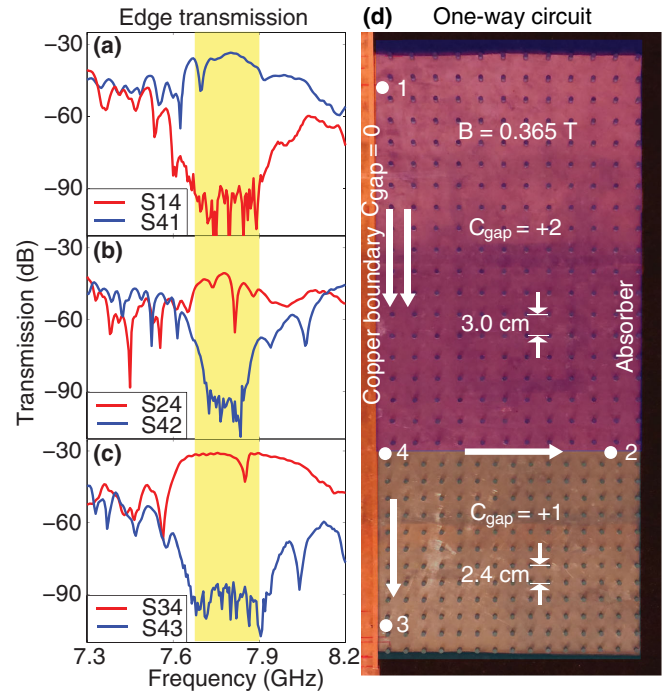


FIG. 3 (color online). Topological one-way circuit implemented using $C_{\text{gap}} = 1$ ($a = 2.4$ cm) and $C_{\text{gap}} = 2$ ($a = 3.0$ cm) photonic crystals. (a)–(c) Transmission plots showing edge transmission between antennas at 1, 2, and 3, and antenna 4 located at the center. Shared bulk band gap for $C_{\text{gap}} = 1$ and $C_{\text{gap}} = 2$ crystals is highlighted in yellow. (d) Experimental configuration illustrating crystals with copper boundary ($C_{\text{gap}} = 0$) on the left and antenna locations 1–4. Arrows indicate the theoretical direction and the number of the edge states at each interface. The transmission data is consistent with predicted edge state directions, which confirms that the upper crystal has $C_{\text{gap}} > 1$.

that in one direction we have a strong band gap, with a signal level at the noise floor of about -100 dB, while in the opposite direction there is 50 to 60 dB more of a transmission. These edge state directions are consistent with the theoretical predictions and prove the existence of $C_{\text{gap}} > 1$ for the upper crystal. The results from Fig. 3 were obtained under an applied magnetic field of 0.365 T, although there was a window extending from approximately 0.32 to 0.4 T, where the $C_{\text{gap}} = 2$ and $C_{\text{gap}} = 1$ band gaps from each crystal were well aligned (see the Supplemental Material [17]).

In conclusion, we experimentally constructed a square lattice ferrimagnetic photonic crystal with a band structure comprising high C_{gap} (-4 to 3) band gaps and measured the dispersion relations of the multimode one-way edge waveguides. Fundamentally, having band gaps with higher gap Chern numbers greatly expands the phases available for topological photonics. These results can potentially enable multimode one-way waveguides with high capacity and coupling efficiencies, as well as many other devices [22–25]. A topological photonic circuit can also be made

by interfacing photonic crystals with various C_{gap} 's, with one-way edge states combining together or splitting off at the junctions. Given the rapidly expanding literature on the QAHE and its analogs for $|C_{\text{gap}}| = 1$ [4,26–31], many more avenues of research are now possible because of the greater range of topological phases that can be investigated. Our approach can be readily extended to other systems of bosonic particles such as magnons [32], excitons [33], and phonons [34,35].

We acknowledge Carl E. Patton, Liang Fu, Bo Zhen, Ido Kaminer, Yichen Shen, Zheng Weng, and Hongsheng Chen for the discussions, Ulrich Becker and Peter Fisher for their assistance with the MIT cyclotron magnet, and Xiangdong Liang for the numerical assistance. S. S. was supported by the MIT Tom Frank Fellowship and the NSF Fellowship. L. L. was supported in part by the MRSEC Program of the NSF under Grant No. DMR-1419807. Q. Y. was supported by the National Natural Science Foundation of China under Grant No. 61322501. The fabrication part of the effort was paid for by the MIT S3TEC EFRC of the U.S. DOE under Grant No. DE-SC0001299. This work was also supported in part by ARO through ISN, Grant No. W911NF-13-D-0001.

*sskirlo@mit.edu

†linglu@mit.edu

- [1] D. J. Thouless, M. Kohmoto, M. P. Nightingale, and M. den Nijs, Quantized Hall Conductance in a Two-Dimensional Periodic Potential, *Phys. Rev. Lett.* **49**, 405 (1982).
- [2] K. v. Klitzing, G. Dorda, and M. Pepper, New Method for High-Accuracy Determination of the Fine-Structure Constant Based on Quantized Hall Resistance, *Phys. Rev. Lett.* **45**, 494 (1980).
- [3] F. D. M. Haldane, Model for a Quantum Hall Effect without Landau Levels: Condensed-Matter Realization of the “Parity Anomaly”, *Phys. Rev. Lett.* **61**, 2015 (1988).
- [4] L. Lu, J. D. Joannopoulos, and M. Soljačić, Topological photonics, *Nat. Photonics* **8**, 821 (2014).
- [5] Z. Wang, Y. Chong, J. D. Joannopoulos, and M. Soljačić, Observation of unidirectional backscattering-immune topological electromagnetic states, *Nature (London)* **461**, 772 (2009).
- [6] C. Chang *et al.*, Experimental observation of the quantum anomalous Hall effect in a magnetic topological insulator, *Science* **340**, 167 (2013).
- [7] G. Jotzu, M. Messer, R. Desbuquois, M. Lebrat, T. Uehlinger, D. Greif, and T. Esslinger, Experimental realization of the topological Haldane model with ultracold fermions, *Nature (London)* **515**, 237 (2014).
- [8] H. Jiang, Z. H. Qiao, W. Liu, and Q. Niu, Quantum anomalous Hall effect with tunable Chern number in magnetic topological insulator film, *Phys. Rev. B* **85**, 045445 (2012).
- [9] J. Wang, B. Lian, H. Zhang, Y. Xu, and S. Zhang, Quantum Anomalous Hall Effect with Higher Plateaus, *Phys. Rev. Lett.* **111**, 136801 (2013).
- [10] C. Fang, M. J. Gilbert, and B. A. Bernevig, Large-Chern-Number Quantum Anomalous Hall Effect in Thin-Film Topological Crystalline Insulators, *Phys. Rev. Lett.* **112**, 046801 (2014).
- [11] S. A. Skirlo, L. Lu, and M. Soljačić, Multimode One-Way Waveguides of Large Chern Numbers, *Phys. Rev. Lett.* **113**, 113904 (2014).
- [12] P. M. Perez-Piskunow, L. E. F. Foa Torres, and G. Usaj, Hierarchy of Floquet gaps and edge states for driven honeycomb lattices, *Phys. Rev. A* **91**, 043625 (2015).
- [13] F. D. M. Haldane and S. Raghu, Possible Realization of Directional Optical Waveguides in Photonic Crystals with Broken Time-Reversal Symmetry, *Phys. Rev. Lett.* **100**, 013904 (2008).
- [14] S. Raghu and F. D. M. Haldane, Analogs of quantum-Hall-effect edge states in photonic crystals, *Phys. Rev. A* **78**, 033834 (2008).
- [15] Z. Wang, Y. D. Chong, J. D. Joannopoulos, and M. Soljačić, Reflection-Free One-Way Edge Modes in a Gyromagnetic Photonic Crystal, *Phys. Rev. Lett.* **100**, 013905 (2008).
- [16] T. Fukui, Y. Hatsugai, and H. Suzuki, Chern numbers in discretized Brillouin zone: Efficient method of computing (spin) Hall conductances, *J. Phys. Soc. Jpn.* **74**, 1674 (2005).
- [17] See Supplemental Material at <http://link.aps.org/supplemental/10.1103/PhysRevLett.115.253901> for a description of the experimental methods, the ferrimagnetic material model, additional mode profile measurements, additional results for the $C_{\text{gap}} = 1$ crystal, and finally further details of the Chern number calculations.
- [18] D. M. Pozar, *Microwave Engineering*, 2nd ed. (Wiley, New York, 1998).
- [19] J. J. Green and F. Sandy, Microwave characterization of partially magnetized ferrites, *IEEE Trans. Microwave Theory Tech.* **22**, 641 (1974).
- [20] Y. Hatsugai, Chern Number and Edge States in the Integer Quantum Hall Effect, *Phys. Rev. Lett.* **71**, 3697 (1993).
- [21] S. Li *et al.*, Probing electric field in an enclosed field mapper for characterizing metamaterials, *Int. J. Antennas Propag.* **2014**, 728756 (2014).
- [22] C. He, X.-L. Chen, M.-H. Lu, X.-F. Li, W.-W. Wan, X.-S. Qian, R.-C. Yin, and Y.-F. Chen, Tunable one-way cross-waveguide splitter based on gyromagnetic photonic crystal, *Appl. Phys. Lett.* **96**, 111111 (2010).
- [23] Y. Yang, Y. Poo, R. Wu, Y. Gu, and P. Chen, Experimental demonstration of one-way slow wave in waveguide involving gyromagnetic photonic crystals, *Appl. Phys. Lett.* **102**, 231113 (2013).
- [24] Y. Poo, R. Wu, Z. Lin, Y. Yang, and C. T. Chan, Experimental Realization of Self-Guiding Unidirectional Electromagnetic Edge States, *Phys. Rev. Lett.* **106**, 093903 (2011).
- [25] J. Fu, J. Lian, R. Liu, L. Gan, and Z. Li, Unidirectional channel-drop filter by one-way gyromagnetic photonic crystal waveguides, *Appl. Phys. Lett.* **98**, 211104 (2011).
- [26] M. Hafezi, E. A. Demler, M. D. Lukin, and J. M. Taylor, Robust optical delay lines with topological protection, *Nat. Phys.* **7**, 907 (2011).
- [27] K. Fang, Z. Yu, and S. Fan, Realizing effective magnetic field for photons by controlling the phase of dynamic modulation, *Nat. Photonics* **6**, 782 (2012).

- [28] A. B. Khanikaev, S. Hossein Mousavi, W.-K. Tse, M. Kargarian, A. H. MacDonald, and G. Shvets, Photonic topological insulators, *Nat. Mater.* **12**, 233 (2013).
- [29] Y. E. Kraus, Y. Lahini, Z. Ringel, M. Verbin, and O. Zilberberg, Topological States and Adiabatic Pumping in Quasicrystals, *Phys. Rev. Lett.* **109**, 106402 (2012).
- [30] M. C. Rechtsman, J. M. Zeuner, Y. Plotnik, Y. Lumer, D. Podolsky, F. Dreisow, S. Nolte, M. Segev, and A. Szameit, Photonic Floquet topological insulators, *Nature (London)* **496**, 196 (2013).
- [31] W. Chen *et al.*, Experimental realization of photonic topological insulator in a uniaxial metacrystal waveguide, *Nat. Commun.* **5**, 196 (2014).
- [32] A. Mook, J. Henk, and I. Mertig, Edge states in topological magnon insulators, *Phys. Rev. B* **90**, 024412 (2014).
- [33] J. Yuen-Zhou, S. K. Saikin, N. Y. Yao, and A. Aspuru-Guzik, Topologically protected excitons in porphyrin thin films, *Nat. Mater.* **13**, 1026 (2014).
- [34] Z. Yang, F. Gao, X. Shi, X. Lin, Z. Gao, Y. Chong, and B. Zhang, Topological Acoustics, *Phys. Rev. Lett.* **114**, 114301 (2015).
- [35] P. Wang, L. Lu, and K. Bertoldi, Topological Phononic Crystals with One-Way Elastic Edge Waves, *Phys. Rev. Lett.* **115**, 104302 (2015).

Supplementary Material

Scott A. Skirlo^{1,*}, Ling Lu^{1,†}, Yuichi Igarashi^{1,2}, Qinghui
Yan^{1,3}, John Joannopoulos¹, and Marin Soljačić¹

¹ Department of Physics, Massachusetts Institute of Technology, Cambridge, MA 02139, USA

² Smart Energy Research Laboratories, NEC Corporation,
34 Miyukigaoka, Tsukuba, Ibaraki 305-8501, Japan

³ The Electromagnetics Academy at Zhejiang University,
Zhejiang University, Hangzhou 310027, China

(Dated: December 14, 2015)

* sskirlo@mit.edu

† linglu@mit.edu

Appendix A: Experimental Methods

The experimental setup, for the bulk and edge transmission measurements, consisted of two parallel copper sheets 1 m by 0.5 m attached to aluminum plates for mechanical stability and were separated by 0.635 cm (0.25 in). In the range of frequencies studied in this work, the sheets only supported modes which had a uniform electric field perpendicular to the plane and the magnetic field in-plane. Even though the experiment was in a 3D system, the modes are effectively uniform in the perpendicular direction and so can be represented by 2D TM simulations. Microwave absorbers placed around the boundary absorbed stray radiation and helped reduce the noise floor of the measurements.

The ferrimagnetic material used to make the crystals was obtained from TCI cermaics (NG-1850) and consisted of rods 0.795 and 0.823 cm in diameter and 0.635 cm tall. The smaller rods were used to construct the 2.4 cm square lattice used for the $C_{gap} = 1$ photonic crystal in Fig. 3, and in the supplementary material. The larger rods were used to construct the 3 cm lattice in Fig. 1-3. The rods had a saturation magnetization ($4\pi M_s$) of 1817 Gauss and a permittivity of 14.23. The loss tangent of the material was $2 \cdot 10^{-4}$ and the gyromagnetic resonance loss width (ΔH) was $170e$. The rods were produced from the same production batch so that the material parameters were uniform. They were machined down to different radii to optimize the overlap and size of the $C_{gap} = 1$ and $C_{gap} = 2$ bandgaps for the splitter experiment presented in Fig. 3. The material had very little hysteresis (and residual magnetization) overall since measurements conducted with increasing, versus decreasing, magnetic field were indistinguishable.

For the mode profile measurements we used a set of lighter and smaller aluminum plates to facilitate easier translation of the upper plate. The aluminum itself is sufficiently conductive for most microwave experiments. The transmitting antenna was mounted to the lower plate, while the receiving antenna was mounted to the upper plate. The upper plate slid along on top of two aluminum bars which were approximately 1 mm higher than the ferrimagnetic rods in the experiment. This gap between the upper plate and the rods was necessary for maintaining smooth translation, and does not invalidate the approximate 2D simulations we used for modeling [1]. The key for a successful mode profile measurement was smooth translation of the upper plate and a consistent metal to metal contact of the supporting bars and the upper plate.

We used a 8719C HP network analyzer for the transmission and mode profile measurements, and a LakeShore Model 410 Gaussmeter for measuring the magnetic field inside the MIT cy-

clotron magnet. Approximately one hundred transmission measurements were made while the magnetic field was swept between 0.03 T and 0.55 T. The frequency data was smoothed over the neighboring 4 points in post-processing. The experimental results presented in Fig. 1 and in the corresponding plot in the supplementary material were calibrated using the S12 parameters calculated for the antennas inside the parallel plate waveguide without the lattice of ferrimagnetic rods. This calibration helped remove the variation in transmission with frequency that results from the intrinsic impedance mismatch of the antenna. All transmission results were normalized by the maximum transmission. No such normalizations and smoothings were carried out for the mode profile results.

Appendix B: Material Model

Under an applied magnetic field, the permeability tensor of the ferrimagnetic garnet takes the following form[2]:

$$[\mu] = \begin{bmatrix} \mu & ik & 0 \\ -ik & \mu & 0 \\ 0 & 0 & \mu \end{bmatrix}$$

Where $\mu = \mu_0(1 + \frac{\omega_0\omega_m}{\omega_0^2 - \omega^2})$ and $k = \mu_0\frac{\omega\omega_m}{\omega_0^2 - \omega^2}$. The gyromagnetic resonance frequency, $\omega_0(= \mu_0\gamma H_{int})$, and $\omega_m(= \mu_0\gamma M)$ are determined by the internal magnetic field H_{int} and the magnetization M where γ is the gyromagnetic ratio. The internal magnetic field, $H_{int}(=H - XM(H))$, is the difference between the external magnetic field H and the demagnetization field $XM(H)$, where X is the geometry-dependent demagnetization factor and $M(H)$ is the magnetization function. For our theoretical calculations we took $M(H) = M_{sat}$, and $H_{int} = H$, since we did not know the low field behavior of $M(H)$. This approximation causes the small offset of about 0.04 T visible between our transmission experiments and calculations in Fig. 1 and Fig. S3.

The diagonal sweeping features in Fig. 1,2, S3-4, and S7-8 that go from low frequency and low magnetic field, to high frequency and high magnetic field are caused by the resonant peak of the effective permeability ($\mu_{eff} = \frac{\mu^2 - k^2}{\mu}$ [2]). The resonance frequency of the effective permeability is $\frac{\sqrt{\omega_0(\omega_0 + \omega_m)}}{2\pi}$. It is important to note that this is different than the gyromagnetic resonance frequency($= \frac{\omega_0}{2\pi}$), which is lower. Bandgaps to the left of this resonance, tend to move upwards in frequency as the magnetic field is increased because the index of the rods($= \sqrt{\epsilon\mu_{eff}}$) is becoming

smaller as μ_{eff} decreases. On the other side of the resonance, the bandgap frequencies tend to shift downward as the magnetic field is decreased because the index is increasing as μ_{eff} increases.

Loss is included in all of the previous calculations by taking $\omega_0 \rightarrow \omega_0 + i\frac{\mu_0\gamma\Delta H}{2}$, where ΔH is the gyromagnetic resonance width.

Appendix C: Mode profile measurement and $C_{gap} = -3$ and -4 comparison to simulation

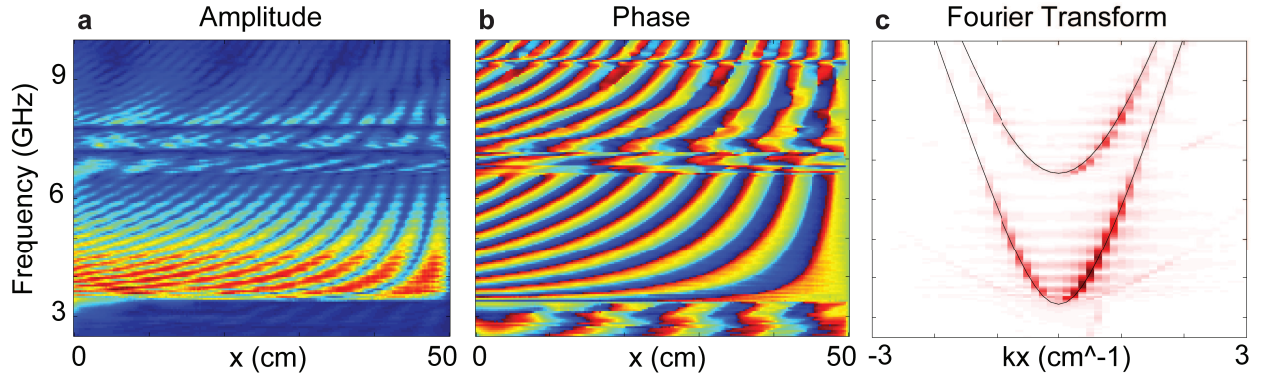


FIG. S1. Phase and amplitude measurements for 4.5 cm by 0.735 cm rectangular waveguide with Fourier transform of calculated mode profile. a) Amplitude measured in waveguide from 0 to 50 cm b) Phase c) Fourier transform of electric field computed from the measured amplitude and phase data. The peaks of the Fourier transform appear in red, and their dispersion matches the theoretical predictions in black. Note that the peaks on the right side (the forward propagating waves) are higher in amplitude. The amplitude of the forward propagating wave is higher than the backward propagating one because of absorption at the end of the waveguide by the microwave absorber.

In Fig. S1 we present the procedure for extracting the dispersion relation of a rectangular waveguide from the mode profile. For this measurement we constructed a 50 cm long rectangular waveguide 0.735 cm tall and 4.5 cm wide. We placed microwave absorbers at the ends of the waveguide which minimized reflections. We first present the raw amplitude and phase data in Fig. S1a and b. The phase and amplitude for the entire range of frequencies was acquired during a single measurement at a specific position in the waveguide. We combined the phase and amplitude data to calculate the electric field along the edge. After we have the total mode profile, we take the Fourier transform to find the peaks in k-space corresponding to the propagating modes. In Fig. S1c, we plot the FT as a function of frequency and wavevector, allowing visualization of the mode

dispersion in the waveguide. The location of the FT peaks matches the theoretically-predicted dispersion relations which are in black. Note there is more energy on the forward propagating branch of the dispersion relation, than the backward propagating one. The phase and amplitude information from the measurement allows us to completely reconstruct the backward and forward propagating modes independently.

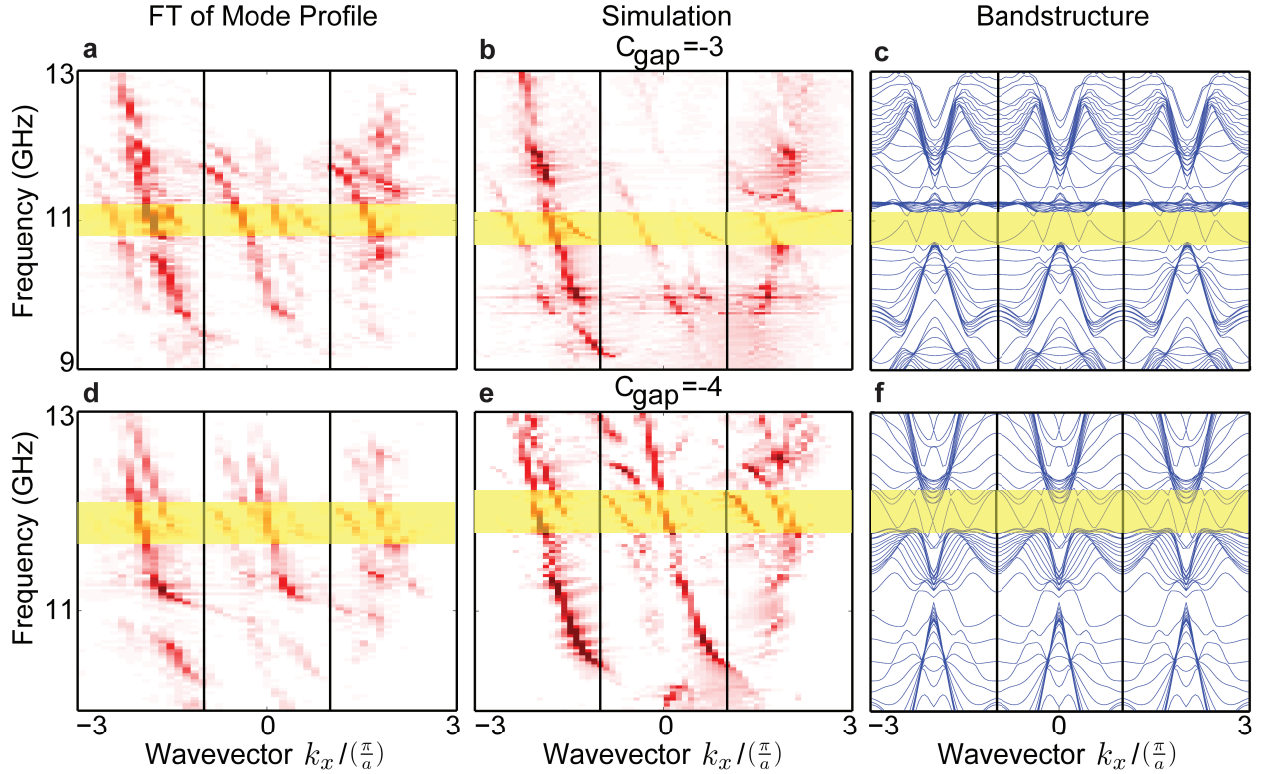


FIG. S2. Fourier Transform of experimental and simulation data compared to computed bandstructure for $C_{gap} = -3$ and -4 from Fig. 2 in main text. Regions of interest are highlighted in yellow. a) FT of experimentally measured mode profile. b) FT of simulated mode profile in geometry closely matching experiment. c) Supercell calculation for bulk and edge bands. Note that in the bandgap we have forward and backward propagating modes, but that each set of these modes is localized to opposite edges. d)-f) The same data sets for $C_{gap} = -4$. The excellent agreement between these figures provides further evidence for the experimental observation of multiple one-way edge modes.

In Fig. S2 we present a comparison between Fourier transforms computed from simulation and experiment, and calculated supercell bandstructures for $C_{gap} = -3$ and -4 from Fig. 2 in the paper. We have highlighted the regions of interest in yellow. In interpreting the results it is important to understand some fundamental features of the Bloch modes propagating in the

lattice. In general the electric field E_z in periodic media can be written as $u(x, y)e^{ikx}$ where $u(x, y) = u(x + a, y)$ is the envelope function and k is the wavevector, we can rewrite this by expanding $u(x, y)$ in its spatial Fourier components:

$$E_z(x, y) = u(x, y)e^{ikx} = \sum_G a_G(y)e^{i(k+G)x} \quad (\text{C1})$$

We can make several important observations about this result. The most important is that we will potentially observe multiple ‘copies’ of a single dispersion relation, shifted by reciprocal lattice vectors G . These copies are clearly visible in the experimental and theoretical results in Fig. S2a and S2b, where we have separated each BZ by vertical black lines.

Another important fact is that the Fourier coefficients a_G are functions of y . This means to reproduce the experimental results precisely that the exact positions of the excitation and measurement antennas have to be known, in addition to the distance between the metal boundary and the photonic crystal. In Fig. S2b we attempted to reproduce the experimental geometry as closely as possible. Despite many variables and nonidealities, the FT from the simulated mode profile bears close resemblance to that measured in experiment, providing further evidence for the observation of multiple one-way modes.

Finally in Fig. S2c we present supercell calculations for the bulk and edge bands. Careful study reveals that many bright-spots in the Fig. S2a and b can be traced back to certain bands which are being excited. Note that the supercell calculations in general include forward and backward propagating modes, but that inside the bandgap, one edge mode dispersion is localized to one end of the computational cell, while the other, oppositely traversing mode is on the opposite side, so in experiment and simulation only one set will be observed.

Appendix D: $C_{gap} = 1$ (a=2.4 cm) photonic crystal

In Fig. S3 and Fig. S4 we present the experimental results for the bottom photonic crystal used for the splitter in Fig. 3, which had a lattice period of 2.4 cm. Fig. S3 shows the agreement between the theoretical gap map, theoretical bulk transmission, and experimental transmission. This crystal was selected because the $C_{gap} = 1$ bandgap (the one to the right of the resonance) occurs in the same frequency and magnetic field ranges as the $C_{gap} = 2$ bandgap in the photonic crystal from Fig. 1 and 2, which we discuss in Appendix D. Fig. S4 shows the edge transmission measurements, and these are consistent with the Chern number and edge mode dispersion from

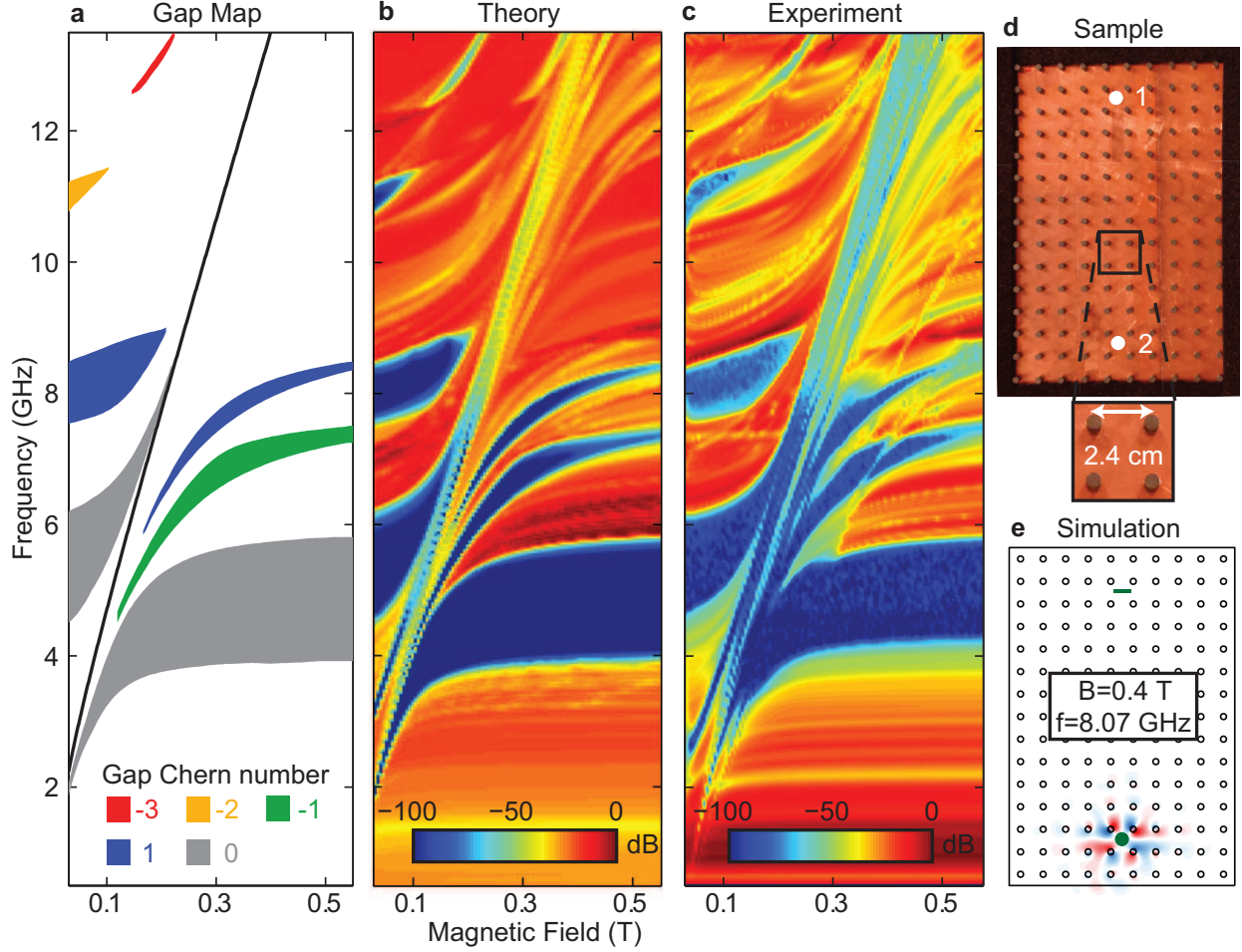


FIG. S3. Comparison of theoretical gap maps and bulk transmission to experimental transmission measurement in a 2D ferrimagnetic photonic crystal for $C_{gap} = 1$ ($a=2.4$ cm) crystal from Fig. 3. a) Theoretical topological gap map as a function of the magnetic field and the frequency with each bandgap labeled by its gap Chern number. The black diagonal line indicates the resonance in the effective permeability (Appendix B) b) Theoretical bulk transmission c) Experimental bulk transmission d) Experimental configuration with the lattice geometry (top metal plate removed). The antenna locations are marked with “1” and “2”. e) Simulation geometry with the green line representing the receiving antenna, and the green circle representing the transmitting antenna.

the edge mode calculations. The large $C_{gap} = 1$ bandgap occurring at low magnetic fields is potentially useful for applications. This bandgap can alternatively potentially be opened without an external magnetic field by using a ferrimagnetic material with remanent magnetization.

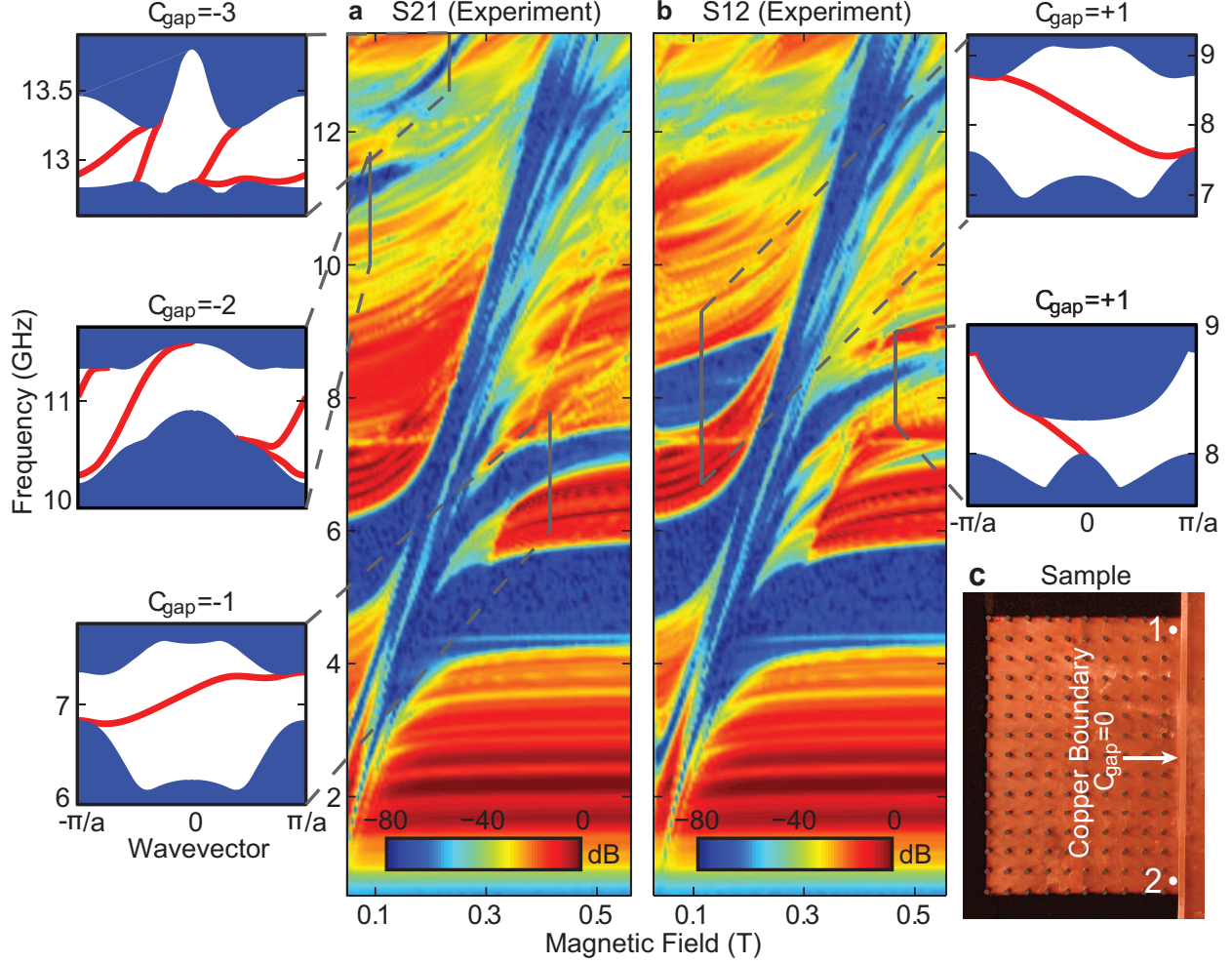


FIG. S4. Experimental edge transmission measurement along copper boundary for $C_{\text{gap}} = 1$ ($a=2.4$ cm) crystal from Fig. 3. a) S21. b) S12. The bandgaps that are nontrivial have direction-dependent edge transmission, because the interface of a nontrivial bandgap with a trivial bandgap (copper boundary) supports one-way modes. In a) and b) this causes the nontrivial bulk bandgaps from Fig. S3 to be present in one direction (e.g. S12) and absent in the other (e.g. S21). The trivial bandgaps around 5 GHz do not support one-way modes, and so do not exhibit direction-dependent transmission. c) Experimental configuration with the antenna locations and the copper boundary. Insets on the left and right side of a) and b) respectively show edge band calculations with the edge modes in red and the bulk bands in blue. Each supercell calculation applies to a) and b) even though each is shown on only one side for clarity. The number of one-way edge modes corresponds to $|C_{\text{gap}}|$ from Fig. S3a, while the sign of C_{gap} is consistent with the theoretical group velocity (from the edge mode dispersion) and the directional transmission in a) and b).

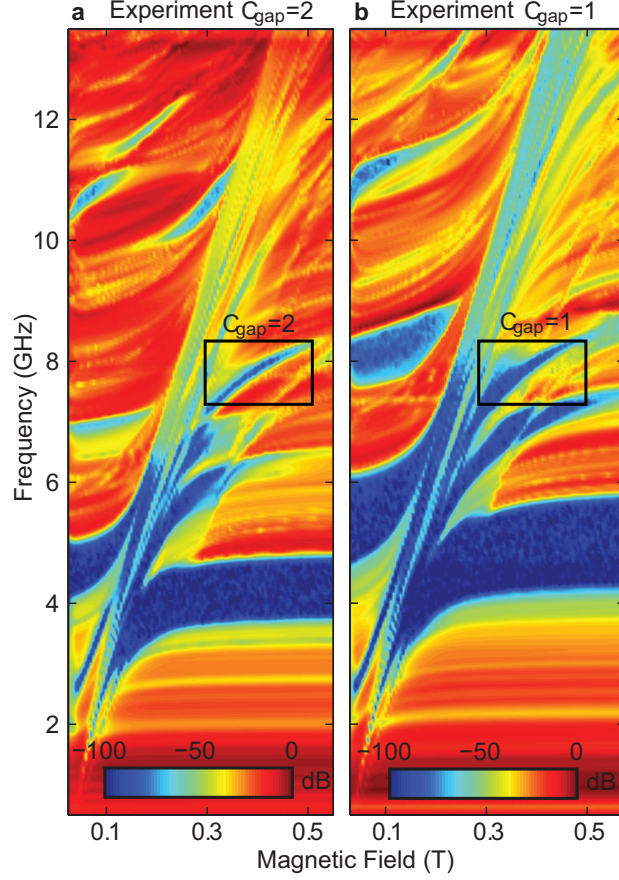


FIG. S5. Alignment of bandgaps for $C_{gap} = 2$ ($a=3.0$ cm) crystal and $C_{gap} = 1$ ($a=2.4$ cm) crystal from Fig. 3 splitter. a) Transmission for $a=3$ cm crystal. The nontrivial $C_{gap} = 2$ bandgap used in the Fig. 3 splitter experiment is boxed in black. b) Transmission for $a=2.4$ cm crystal. The nontrivial $C_{gap} = 1$ bandgap used in the Fig. 3 splitter experiment is boxed in black. The $C_{gap} = 2$ bandgap and $C_{gap} = 1$ bandgap from each crystal show good frequency alignment over a range of magnetic fields from 0.32 T to 0.4 T

Appendix E: Bandgap alignment between $C_{gap} = 2$ ($a=3.0$ cm) and $C_{gap} = 1$ ($a=2.4$ cm) photonic crystals

We designed each crystal in the Fig. 3 splitter experiment so that a nontrivial $C_{gap} = 2$ bandgap from one crystal would be well aligned at a certain magnetic field with the $C_{gap} = 1$ bandgap of another crystal for a sufficiently large range of frequencies. The $C_{gap} = 2$ crystal was studied in Fig. 1 and 2, and consisted of a square lattice of rods with lattice constant 3 cm. The $C_{gap} = 1$ crystal was studied in Fig. S3 and S4, and consisted of a square lattice of rods with lattice constant

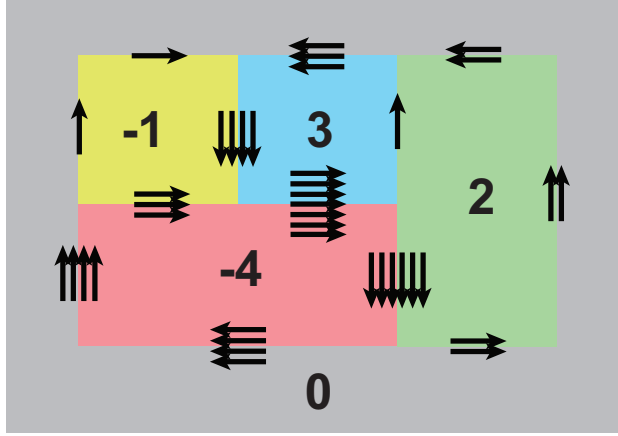


FIG. S6. One-way Topological Photonic Circuit. Photonic one-way circuit which can be constructed using the topological bandgaps we found. Arrows represent one-way edge modes and each crystal is labeled by its gap Chern number.

2.4 cm. The transmission measurements showing the bandgaps of each crystal are presented in Fig. S5 with the location of each bandgap highlighted with a black box. For the $C_{gap} = 1$ bandgap and the $C_{gap} = 2$ bandgap, there is significant frequency overlap between the bandgaps for magnetic fields between approximately 0.32 T and 0.4 T. This overlap was achieved through theoretical calculations and experimental tuning of the lattice constant.

Appendix F: One-way Topological Photonic Circuit

We include an example of a topological photonic circuit using the topological bandgaps we found in Fig. S6. We assume in this figure that each topological bandgap for each topological “block” is perfectly aligned in frequency with all of the others. Each topological “block” is labeled with its gap Chern number. At the junction between three bulk domains, one-way edge states merge together or branch off, enabling new device functionalities as signal combiners and photonic logic gates immune to backscattering from manufacturing imperfections.

Appendix G: Chern Number Sums

In Fig. S7 and S8 we present the topological gap maps for the photonic crystals we constructed along with insets illustrating the detailed bandstructure at the minimum and maximum magnetic fields. Each band in the insets is labeled with its Chern number. The sum of the Chern numbers

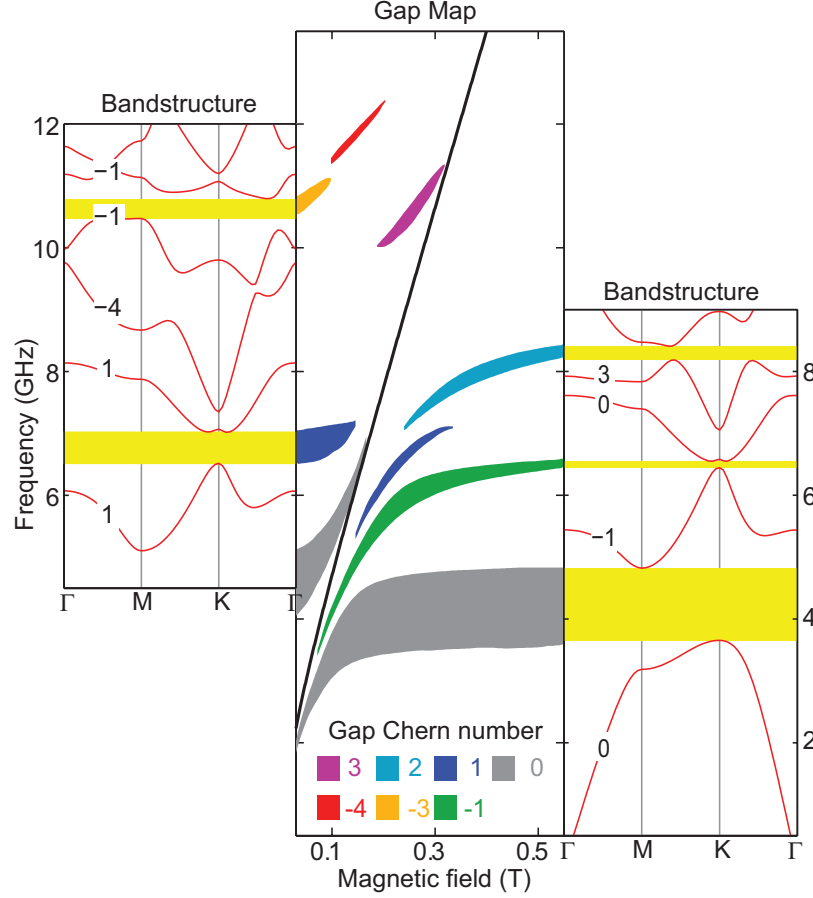


FIG. S7. Calculation of C_{gap} by summing Chern numbers below bandgap for the $C_{gap} = 2$ ($a=3.0$ cm) crystal from Fig. 1,2, and 3. On each side of the gap map we have included bulk bands labeled with their Chern numbers. The sum of the Chern numbers of bands below a given complete bandgap is the gap Chern number.

of all bands below a given bandgap is the gap Chern number[3]. We labeled each band in the gap map with its gap Chern number determined with this rule. The insets were computed using fixed point iteration, while the gap map was computed using transmission calculations as detailed in Appendix G.

Appendix H: Numerical Methods

The bandstructure and transmission plots in this work were calculated using COMSOL which utilizes the finite element method. The Chern numbers of each bulk band were calculated using a custom made finite-difference frequency-domain code.

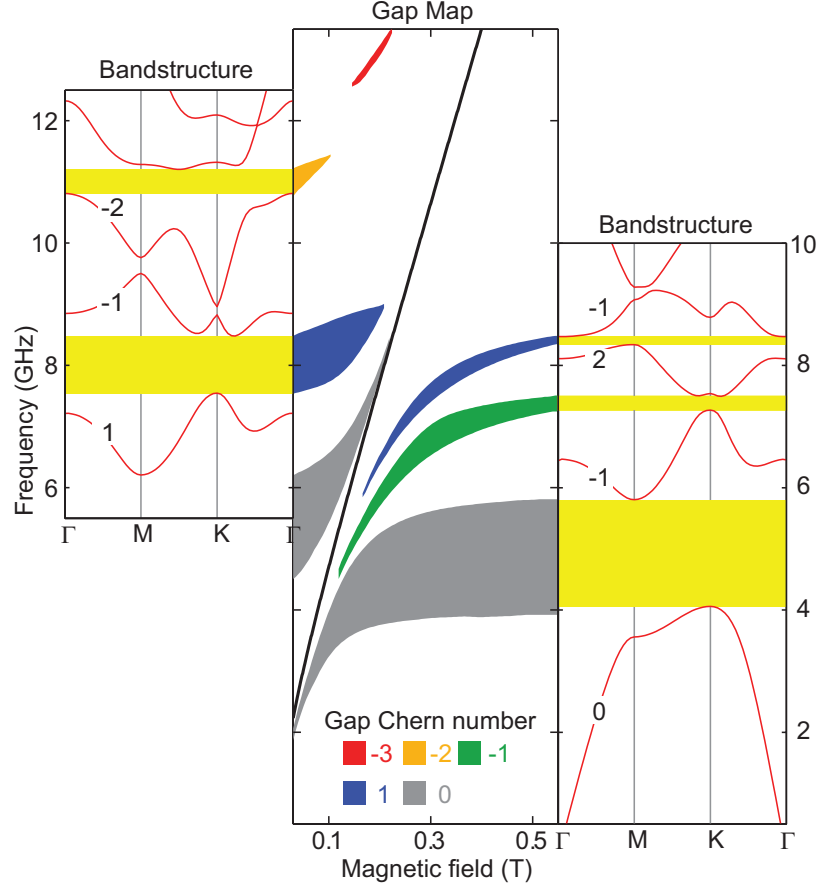


FIG. S8. Calculation of C_{gap} by summing Chern numbers below bandgap for the $C_{gap} = 1$ ($a=2.4$ cm) crystal from Fig. 3, S3, and S4. On each side of the gap map we have included bulk bands labeled with their Chern numbers. The sum of the Chern numbers of bands below a given complete bandgap is the gap Chern number.

For the bandstructure calculations, we solved a Hermitian eigenproblem of the following form in COMSOL.

$$\nabla \times (\mu^{-1} \nabla \times \vec{E}) = \epsilon \omega^2 \vec{E}$$

Since ferrimagnetic materials are dispersive (μ depends on ω), this is a nonlinear eigenproblem. Even though COMSOL can only solve linear eigenproblems, we can still find the solution to the nonlinear eigenproblem using fixed-point iteration. In this method the material parameters are evaluated at a trial frequency so that the normal linear eigenvalue problem can be solved. The new solution is used to evaluate the material parameters again, and if the initial guess is close enough, the frequency will converge with enough iterations. We applied fixed-point iteration to calculate the bandstructures in Appendix F.

For the supercell calculations in the paper, the linear eigenvalue problem was solved with material parameters evaluated at the midgap frequency. Material dispersion will cause the bandgaps to become smaller without effecting the topological properties. Consequently we did not include dispersion in the supercell calculations since they contained a large number of bands and would consequently take too many computing hours. The supercell calculations were computed using 15 unit cells of the photonic crystal joined at the ends either with periodic boundary conditions, in the case of the bulk calculations, or metallic boundary conditions, for edge-mode calculations.

The transmission was also calculated with COMSOL by solving for the time-harmonic solution at a given frequency and magnetic field. For these calculations the source “antenna” was represented by three point current sources of equal magnitude in the normal direction within a single unit cell of the crystal. The receiving antenna was represented by a short line on the other side of the crystal over which the power was integrated. The boundaries of the crystal were padded with perfectly matched layers. The effects of material loss and material dispersion were included in the calculation.

Additional transmission simulations were conducted to find the gap map in Fig. 1a and in the supplementary material. In order to sample the full k-space, the receiving boundary was expanded to receive all unique incoming waves from the current sources. The low transmission regions were identified and used to create the gap map. The locations of these gaps are consistent with the bandstructure calculations as shown in Fig. S7 and Fig. S8. Here the fixed-point iteration and transmission methods show good agreement in regimes of low dispersion and loss.

-
- [1] Li, Sucheng, et al. Probing Electric Field in an Enclosed Field Mapper for Characterizing Metamaterials. *Int. J. Antennas Propag.* 2014 (2014).
 - [2] Pozar, D.M. *Microwave Engineering* 2nd edn (Wiley, 1998).
 - [3] Hatsugai, Y. Chern number and edge states in the integer quantum Hall effect. *Phys. Rev. Lett.* **71**, 3697 (1993).